Bonding properties of Rubik's-cube-like Slater-Pauling Heusler semiconductors for thermoelectrics

Zhuoyang Ti,[1,2] Jianbo Zhu,[3,4] Shuping Guo,[5] Jingyu Li,[6] Xiaobing Liu,[3] and Yongsheng Zhang[3,*]

[1]*Key laboratory of Materials Physics, Institute of Solid State Physics, HFIPS, Chinese Academy of Sciences, Hefei 230031, China*

[2]*Science Island Branch of Graduate School, University of Science and Technology of China, Hefei 230026, China*

[3]*Advanced Research Institute of Multidisciplinary Sciences, Qufu Normal University, Qufu, Shandong Province 273165, China*

[4]*State Key Laboratory of Advanced Welding and Joining, Harbin Institute of Technology, Harbin 150001, China*

[5]*Institute for Theoretical Solid State Physics, Leibniz IFW Dresden, 01069 Dresden, Germany*

[6]*Spallation Neutron Source Science Center, Dongguan 523803, China*

(Received 26 June 2023; accepted 18 October 2023; published 15 November 2023)

Heusler compounds [XYZ for half-Heusler (HH) and XY_2Z for full-Heusler (FH)] with semiconducting behaviors have been long suggested as promising high-performance thermoelectric (TE) materials. Recently, some off-stoichiometry Heusler compounds (such as the mixture of HH and FH compounds) were predicted as semiconductors as well, which disobey the traditional valence electron count rule and are named Slater-Pauling (S-P) semiconductors. However, the bonding behaviors in these S-P semiconductors and the relationship between the geometry and TE properties are still unclear. Therefore, focusing on the Ti-Fe-Sb and *M*-Co-Sn (*M* = Ti, Zr, Hf) Heusler systems, we theoretically predict several thermodynamically stable off-stoichiometry Heusler compounds ($TiFe_{1.5}Sb$ and $MCo_{1.33}Sn$) and clarify the bonding behaviors of those S-P semiconductors. From the geometry analysis of these compounds, in addition to the HH and FH local geometries, the disorder occupation of Y atoms (Fe or Co) in the lattice also induces the defective-HH and defective-FH substructures, and the stacking style forms second- and third-order Rubik's-cube-like structures. This unique stacking arrangement (or the Y occupations) not only plays an essential role in the electron redistribution in the lattice to form the band gap but also lowers the acoustic Debye temperature and strengthens the anharmonic to suppress the lattice thermal conductivity. Owing to the high power factor and low thermal conductivity, the calculated zT value of *p*-type $ZrCo_{1.33}Sn$ can reach 0.54 at 1000 K. This value could be further optimized using defect engineering. Thus, we not only elucidate the underlying mechanism behind the emergence of S-P semiconductors in Heusler systems but also offer valuable insight into experimental exploration and discovery of S-P semiconductors exhibiting superior TE performance.

DOI: 10.1103/PhysRevB.108.195203

I. INTRODUCTION

Since the discovery of Heusler alloys [1], research on Heusler compounds has focused on two stoichiometries of half-Heusler (HH: XYZ) and full-Heusler (FH: XY_2Z) compounds. The family of Heusler alloys is very attractive due to rich electronic structures within similar crystal structures [2–5]. HH and FH both have face-centered cubic sublattices. In the HH template, X, Y, and Z are located at the Wyckoff positions of 4*a* (0,0,0), 4*c* ($\frac{1}{4}$, $\frac{1}{4}$, $\frac{1}{4}$) and 4*b* ($\frac{1}{2}$, $\frac{1}{2}$, $\frac{1}{2}$), respectively. If the 4*d* ($\frac{3}{4}$, $\frac{3}{4}$, $\frac{3}{4}$) position is also occupied by the Y atom, the FH compound with the XY_2Z composition can be formed. Research on Heusler compounds has focused on stoichiometries of HH (XYZ), FH (XY_2Z), inverse Heusler (X_2YZ) [6], and quaternary Heusler ($XYY'Z$) [7] compounds. Due to their excellent thermal stability and mechanical properties, Heusler alloys are suggested as thermoelectric (TE) materials in the high-temperature range [5]. The efficiency of a TE material is quantified by the TE figure of merit $zT = S^2\sigma T/(\kappa_e + \kappa_l)$, where S, σ, T, κ_e, and κ_l are the Seebeck coefficient, electrical conductivity, absolute temperature, electronic thermal conductivity, and lattice thermal conductivity, respectively. Optimizing the zT value requires maximizing the power factor (PF = $S^2\sigma$) and minimizing the thermal conductivity κ [8].

Traditionally, Heusler compounds with semiconducting behaviors have been promising TE materials. Such behaviors of HH and FH systems are associated with their electronic structures, such as the valence electron counts (VECs) [9]. The well-known 18-electron (18e) rule in the HH (XYZ) compounds is: If the valence electrons of all elements in the HH system are added up to 18 (e.g., NbFeSb = 5[Nb($s^2\,d^3$)] + 8[Fe ($3d^6\,4s^2$)] + 5[Sb($s^2\,p^3$)]), the system shows stable semiconductor behavior. In the system of FH (XY_2Z), it is the 24-electron (24e) rule for a semiconductor. For HH alloys, *M*NiSn, *M*CoSb (*M* = Ti, Zr, Hf) and *R*FeSb (*R* = V, Nb, Ta) are the most investigated TE compounds [10]. They usually exhibit a high Seebeck coefficient, high electrical conductivity, and a high PF. However, a common obstacle to achieving high TE efficiency in HH is their relatively high thermal conductivity (>15 W/mK at 300 K) [11–14]. Thus, authors of several studies have demonstrated that introducing grain boundaries in polycrystalline samples [15,16] and isoelectronic sublattice alloying [17,18] can drastically reduce the lattice thermal conductivity without detriment to

*yshzhang@qfnu.edu.cn

electrical conductivity. With these efforts, the peak zT values obtained from *n*-type *M*NiSn [19,20] and *p*-type *M*CoSb [21,22] and *R*FeSb [23,24] HH compounds are above unity. In contrast to the HH compounds, only a few FH materials are semiconductors and have thus attracted limited attention as TE materials [25–27]. The most widely studied FH semiconductor is VFe_2Al, which shows remarkable TE properties in thin film materials [25]. Garmroudi *et al.* [28] achieved a $PF_{max} = 10.3\,mW/mK^2$ by Ta substitution at V in VFe_2Al.

In addition to the 18e XYZ and 24e XY_2Z Heusler compounds, Heusler compounds with the off-stoichiometric (the mixture of non-18e HH and non-24e FH) can be found in the Inorganic Crystal Structure Database [29] and Ref. [9], albeit in small numbers. The TE properties of some off-stoichiometric or defective Heusler compounds have been explicitly investigated, such as introducing X-deficient (e.g., $Nb_{0.8}CoSn$ [30,31], $Ti_{0.75}NiSb$ [32]), Y-interstitial ($TiFe_{1.5}Sb$ [33,34], $MCo_{1.5}Sn$ (M = Ti, Zr, Hf) [35], $MRu_{1.5}Sb$ [36–38], $MNi_{1+x}Sn$ [39–43]), or substitutes on the X and Y sites (e.g., double HH [14,44,45]) in HH alloys. From the heat transport, the introduction of defects on the X and Y sites in a perfect lattice leads to a significant reduction in the thermal conductivity ($\kappa_l \sim 1.8$ W/mK of $Nb_{0.83}CoSb$ at 1123 K and $\sim$1.7 W/mK of $TiRu_{1.2}Sb$ at 811 K), which can improve the corresponding TE properties ($zT \sim 0.9$ for $Nb_{0.83}CoSb$ at 1123 K, $zT \sim 0.4$ for $TiRu_{1.2}Sb$ at 811 K [31,38]). For the electronic structures, some off-stoichiometry compounds interestingly show semiconductor behavior, such as the Y-interstitial Heusler phases with $XY_{1+n}Z$ ($0 < n < 1$): $TiFe_{1.5}Sb$ [33,34] and $MRu_{1.5}Sb$ (M = Ti, Zr, Hf) [36–38]. This semiconductor behavior cannot be explained by the above 18e/24e simple rules: $TiFe_{1.5}Sb$ and $MRu_{1.5}Sb$ have VEC of 21 ($4\,[Ti/Zr/Hf\,(3d^2\,4s^2)] + 1.5 \times 8[Fe\,(3d^6\,4s^2)/Ru\,(4d^7\,5s^1) + 5\,Sb\,(5s^2\,5p^3)]$), neither 18 nor 24.

Researchers related these Heusler systems to the general Slater-Pauling (S-P) rule [46–48]. According to the rule, an average of 6 electrons of each atom in the ternary Heusler system will lead to semiconductor behavior, which is a so-called *S-P semiconductor* [37]. For the HH and FH systems, they have 3 and 4 atoms in their stoichiometries (XYZ and XY_2Z), respectively. Following the S-P rule, the number of valence electrons of $3 \times 6 = 18$ and $4 \times 6 = 24$ are the semiconductor criteria for HH and FH, respectively, i.e., the well-known 18e and 24e rules. For the off-stoichiometry $TiFe_{1.5}Sb$ and $MRu_{1.5}Sb$ compounds, their 21 valence electrons can exactly split as $6 + 1.5 \times 6 + 6 = 21$ using their stoichiometry $XY_{1.5}Z$, indicating S-P semiconductors. However, for the $TiFe_{1.33}Sb$ and $MCo_{1.5}Sn$ compounds, they do not satisfy the S-P rule [the average electrons of each atom are $(4 + 1.33 \times 8 + 5)/(1 + 1.33 + 1) = 5.9$ and $(4 + 1.5 \times 9 + 4)/(1 + 1.5 + 1) = 6.14$, respectively, not 6], exhibiting metallic character [35,49]. The advantage of these S-P HH semiconductors is using the self-doping to achieve *p*- or *n*-type semiconductors within the same element framework. For example, in the $TiFe_{0.5}Ni_{0.5}Sb$ HH compound [50], tuning the ratio of Fe and Ni (self-doping not extrinsic doping) can lead to both *p*- and *n*-types. Although the S-P rule provides a straightforward relationship between the Heusler system and semiconductor behavior, it does not provide a comprehensive analysis of electronic structures, such as the electron transfer and bonding. In addition, for the off-stoichiometry Heusler compound ($XY_{1+n}Z$), which contains more or fewer Y atoms than HH and FH compounds, respectively, the effect of the Y occupations on the Heusler stability is still unclear. Therefore, it is crucial to conduct a systematic investigation of the stable off-stoichiometry Heusler phases, exploring their electron structures, structure stabilities, and possible TE properties.

In this paper, for the Ti-Fe-Sb and *M*-Co-Sn (M = Ti, Zr, Hf) Heusler systems, we identify the thermodynamically stable phases of $TiFe_{1.5}Sb$ and $MCo_{1.33}Sn$, which are S-P semiconductors. In addition to the well-known HH and FH local geometries, these structures contain defective-HH (DH) and defective-FH (DF) substructures due to the partial occupation of Y atoms (Fe or Co) at the 4*d* Wyckoff position. Such HH, FH, DH, and DF local geometry stacking forms the interesting second- and third-order Rubik's-cube-like structures in $TiFe_{1.5}Sb$ and $MCo_{1.33}Sn$, respectively. The stacking arrangement (or the arrangement of Y atoms) attributes the electron redistribution within the HH and FH substructures, leading to the shift of the Fermi energy level within the band gap. On the other hand, the unique cube significantly suppresses the acoustic phonon branches, lowers the acoustic Debye temperature, and strengthens the anharmonicity. Consequently, the thermal conductivity of $MCo_{1.33}Sn$ (12.5 W/mK for $TiCo_{1.33}Sn$, 11.6 W/mK for $ZrCo_{1.33}Sn$, and 10.8 W/mK for $HfCo_{1.33}Sn$ at 300 K) is much lower than that of the traditional Heusler compounds [NbFeSb (16 W/mK [24]) and VFe_2Al (38 W/mK [51])]. In combining the electrical properties, we find that the zT value of 0.54 can be achieved in the $ZrCo_{1.33}Sn$ Heusler compound. Its TE properties can be further increased using defect engineering. In this paper, we not only explain the origin of the Heusler S-P semiconductor gap using the electronic structures but also provide insight into the experimental discovery of more S-P semiconductors with superior TE performance.

II. METHODOLOGY

A. Density functional theory

All density functional theory (DFT) [52] calculations are performed using VASP within the framework of the projector augmented wave [53]. The generalized gradient approximation of Pardew, Burke, and Ernzerhof (GGA-PBE) [54] is used to understand the electronic exchange-correlation functional. To accurately calculate the ground-state energy, spin-polarization effects are included in the DFT calculations. An energy cutoff of 400 eV is used to truncate the plane-wave function, and the Monkhorst-Pack [55] scheme is used for integration over the Brillouin zone (BZ) with *k*-point meshes of $8 \times 8 \times 8$ for $TiFe_{1.5}Sb$ and $8 \times 8 \times 3$ for $MCo_{1.33}Sn$. All structures are relaxed with respect to all the forces and components of the tensors < 0.01 eV/Å and 0.2 kbar, respectively. The crystal orbital Hamilton population (COHP) calculations are performed to analyze the orbital interactions (bonding vs antibonding) between atoms using the LOBSTER software [56].

B. Cluster expansion

The cluster expansion (CE) has long been used to predict the crystal structures of distinct phases [14,44,57–59]. The formation energy of any configuration ϕ in a pseudobinary alloy $A_{1-x}B_x$ can be defined as

$$E_f(\phi) = \frac{E(\phi) - xE_A - (1-x)E_B}{N_{\text{mix}}}, \tag{1}$$

where $E(\phi)$, E_A, and E_B are the DFT total energies of the mixed structure and the pure constituents A and B, respectively. Here, x is the composition of A, and N_{mix} is the number of mixing atoms. The total energy of any configuration can be written exactly as a series expansion through discrete interactions [effective cluster interactions (ECIs)] within clusters:

$$E_f(\phi) = J_0 + \sum_{i}^{\text{sites}} J_i\sigma_i + \sum_{i\neq j}^{\text{pairs}} J_{ij}\sigma_i\sigma_j + \sum_{i\neq j\neq k}^{\text{triples}} J_{ijk}\sigma_i\sigma_j\sigma_k + \cdots, \tag{2}$$

where in a binary alloy $(A_{1-x}B_x)$, $\sigma_{i,j,k} = 1$ or -1 indicate whether site i in the cluster is occupied by an atom of type A or B, respectively. The coefficients $J_{i,j,k}$ are the ECIs for a cluster (e.g., pairs, triplets, etc). Generally, the expansion of ECI [Eq. (2)] must be truncated after a finite number of terms, and the leave-one-out cross-validation (CV) [60] is used to quantify the accuracy of clusters used in the expansion. After fitting >90 ordered configurations, the CVs of $TiFe_{1+x}Sb$, $TiCo_{1+x}Sn$, $ZrCo_{1+x}Sn$, and $HfCo_{1+x}Sn$ are <15 meV per mixing atom, and the ground-state line or the convex hull is established to make sure that no new low-energy structures are below the line.

C. Electrical transport properties

The electrical transport properties [the Seebeck coefficient (S) and electrical conductivity (σ/τ)] are calculated by solving the Boltzmann transport equations (BTEs), as implemented in the BOLTZTRAP code [61,62]. To assess the TE conversion quality, the constant relaxation time approximation (CRTA) is used, which has been widely used in the electronic transport calculations of HH [63,64] and FH alloys [65]. For simplicity, the relaxation time τ_{CRTA} is set as 10^{-14} s, as used in Ref. [61]. To verify the accuracy of the value, we estimate the electronic relaxation times using momentum relaxation time approximation (MRTA) [66]. This methodology includes the elastic scattering mechanism (acoustic deformation potential scattering or ionized impurity scattering) and inelastic scattering mechanism (polar optical phonon scattering). Our calculation shows that the electron relaxation time is $\sim 10^{-14}$ s for the experimentally suggested compounds $TiFe_{1.5}Sb$ and $TiCo_{1.33}Sn$ (for detail of the calculations, see the Supplemental Material [67]). Therefore, it is reasonable and convenient to use the constant $\tau_{\text{CRTA}} = 10^{-14}$ s to evaluate the electrical properties of these materials. A high density of k points (100 Å) is used to obtain the fine electron band structures for accurate electrical transport properties. According to the rigid band approximation, the effective mass (m_d^*) of the density of states (DOS) is obtained by fitting the DOS near the Fermi level:

$$\text{DOS}(E) = \frac{1}{2\pi^2}\left(\frac{2m_d^*}{\hbar^2}\right)^{3/2} E^{1/2}, \tag{3}$$

where E is the electronic energy and $\hbar$ is the reduced Planck constant. The band effective mass (m_b^*) is calculated using the band structures by fitting $m_b^* = \sqrt[3]{m_x^* m_y^* m_z^*}$, where m_x^*, m_y^*, and m_z^* are the effective masses along the x, y, and z directions at one specific k point in the band structures, respectively.

D. Lattice thermal conductivity

The phonon dispersions are calculated by using density functional perturbation theory [68] with the PHONOPY [69] code. To get the converged thermal properties, $2 \times 2 \times 2$ supercells (56 atoms for $TiFe_{1.5}Sb$ and 80 atoms for $TiCo_{1.33}Sn$ and $ZrCo_{1.33}Sn$) and a $3 \times 3 \times 1$ supercell (90 atoms for $HfCo_{1.33}Sn$) are used. The supercells are constructed based on the cluster expansion predicted crystal structures. To determine the three-phonon (P3) scattering process, we use the THIRDORDER.PY [70] code to obtain the third-order interatomic force constants. The phonon BTEs are solved with the SHENGBTE [71] code, and the BZ integration is performed on a $12 \times 12 \times 12$ grid.

III. RESULT AND DISCUSSIONS

A. Phase diagrams and crystal structures of $TiFe_{1+x}Sb$ and $MCo_{1+x}Sn$ (M = Ti, Zr and Hf)

To access the stable ordered structures in the four kinds of HH-FH mixtures [$TiFe_{1+x}Sb$ and $MCo_{1+x}Sn$ (M = Ti, Zr, Hf)], we use the CE method to construct their pseudobinary phase diagrams (Fig. 1). In the HH (XYZ) lattice system, the atomic positions of X, Y, and Z are located at the Wyckoff sites of 4a (0,0,0), 4c ($\frac{1}{4}$, $\frac{1}{4}$, $\frac{1}{4}$) and 4b ($\frac{1}{2}$, $\frac{1}{2}$, $\frac{1}{2}$), respectively, while the 4d site ($\frac{3}{4}$, $\frac{3}{4}$, $\frac{3}{4}$) remains vacant. When the Y atom fully occupies the 4d site, the FH (XY_2Z) will be formed. Therefore, the comparison of atomic occupations between FH and HH depends on whether the 4d site is occupied or not. During the CE procedure, the Y atom is partially occupied at (or taken from) the 4d site in the HH (or FH) lattice. In other words, partial Y atoms at the 4d site in the FH lattice will move to the empty 4d site in the HH lattice. In the phase diagram, the left ($x = 0$) and right ($x = 1$) endpoints represent the 17-electron HH compounds (TiFeSb and MCoSn) and 25/26-electron FH compounds ($TiFe_2Sb$/MCo_2Sn), respectively. Relative to HH and FH compounds, the DFT-calculated formation energies of all mixed configurations are negative, confirming that all predicted structures are stable compared with the two endpoints (HH and FH); then the convex hull can be established (the black dashed line with yellow circles). For these two kinds of systems ($TiFe_{1+x}Sb$ and $MCo_{1+x}Sn$), the most stable structures are $TiFe_{1.5}Sb$ and $MCo_{1.33}Sn$. The correctly predicted ground-state phases depend on the stability of the endpoint phases. According to the Open Quantum Materials Database [72], the FH compounds of MCo_2Sn (M = Ti, Zr, Hf) are all stable. However, the three endpoints of TiFeSb, $TiFe_2Sb$, and TiCoSn are unstable. They thermodynamically decompose into the corresponding compounds: TiFeSb $\rightarrow$($\frac{1}{3}$ TiSb + $\frac{1}{3}Ti_2Fe_3Sb_2$), $TiFe_2Sb \rightarrow$($\frac{1}{2}$ Fe + $\frac{1}{2}Ti_2Fe_3Sb_2$), and

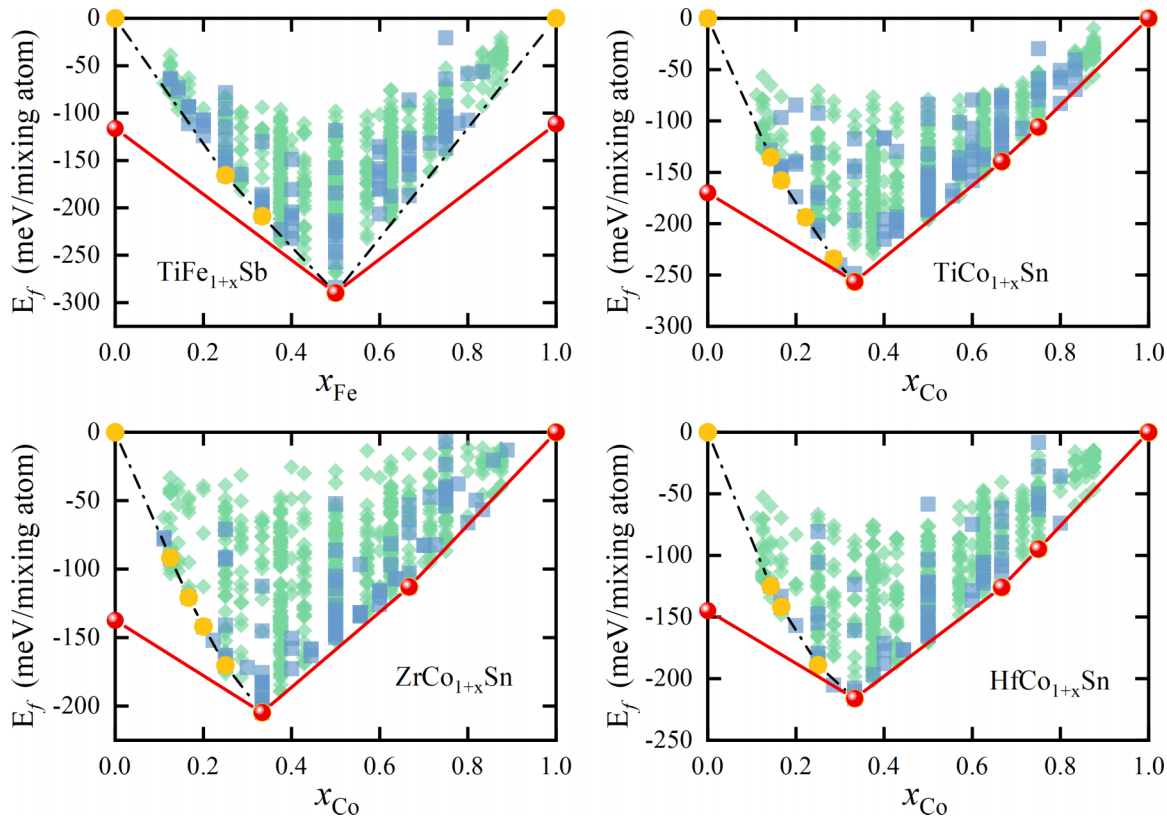

FIG. 1. Theoretically predicted phase diagrams of (a) $TiFe_{1+x}Sb$, (b) $TiCo_{1+x}Sn$, (c) $ZrCo_{1+x}Sn$, and (d) $HfCo_{1+x}Sn$. The formation energies calculated by density functional theory (DFT) are shown as the blue squares. The corresponding cluster expansion predicted energies are shown as the green diamonds. The black dashed line and red solid line represent the convex hull using the ideal cubic half-Heusler (HH)/full-Heusler (FH) phase and their corresponding phase separations of the two endpoints, respectively. The yellow and red points represent the ground states on the corresponding ground-state lines.

$TiCoSn \rightarrow (\frac{1}{3}Ti_2Co_3Sn_2 + \frac{1}{24}Ti_2Sn_3 + \frac{1}{24}Ti_6Sn_5)$. In addition, the ground states of ZrCoSn and HfCoSn crystalize in the hexagonal structure ($P\bar{6}2m$) rather than the Heusler-like cubic structure ($F\bar{4}3m$). Accordingly, we calculate the energy of the decomposed or stable compounds (TiFeSb, $TiFe_2Sb$, TiCoSn, ZrCoSn, and HfCoSn), and they are 116.3, 111.3, 169.9, 137.4, and 144.9 meV per mixing atom below the corresponding Heusler-like cubic structures, respectively. The new convex hulls thus are rebuilt using these low energies (the red lines in Fig. 1). We notice that the stable compounds near the left endpoint (the HH phase) in the previous convex hull are not stable in the new convex hull. The theoretically predicted stable compounds are $TiFe_{1.5}Sb$, $TiCo_{1.33}Sn$, $TiCo_{1.67}Sn$, $TiCo_{1.75}Sn$, $ZrCo_{1.33}Sn$, $ZrCo_{1.67}Sn$, $HfCo_{1.33}Sn$, $HfCo_{1.67}Sn$, and $HfCo_{1.75}Sn$ (Fig. 1). (Since $Ti/Zr/HfCo_{1.67}Sn$ and $Ti/HfCo_{1.75}Sn$ show metallic properties, they are not discussed in detail, and their structure information can be found in Table S2 and Fig. S2 in the Supplemental Material [67].) The results show that the predicted $TiFe_{1.5}Sb$ phase remains as the most stable compound in the Ti-Fe-Sb system, consistent with previous experimental synthesis [33]. However, regarding the $MCo_{1+x}Sn$ (M = Ti, Zr, Hf) system, $MCo_{1.33}Sn$ is the most stable phase, which is different from experimentally suggested $MCo_{1.5}Sn$ [35]. The stability discrepancy between the theoretical predictions and experimental measurements may be due to the finite temperature effects on the Gibbs energy, including the atomic vibrations and the possible configurational entropy due to the Co random occupations.

The crystal structures of theoretically predicted ground state $TiFe_{1.5}Sb$ and $MCo_{1.33}Sn$ (M = Ti, Zr, Hf) are shown in Fig. S1 and Table S1 in the Supplemental Material [67] (for the lattice structures and atom positions). The ground state $TiFe_{1.5}Sb$ has a space group of $R3m$ ($a = b = 4.218$ Å, $c = 20.498$ Å), which agrees with the previous theoretical results [33]. The $MCo_{1.33}Sn$ has a space group of $P3m1$ ($a = b = 4.284$ Å, $c = 10.495$ Å). We compute the x-ray powder diffraction (XRD) for the predicted ordered S-P structures and the corresponding HH and FH (Fig. S4 in the Supplemental Material [67]). From the XRD patterns, we notice that the predicted S-P structures keep the most important XRD peaks from the HH and FH structures, suggesting that they nearly maintain the HH/FH lattice. Additionally, some distinct XRD peaks in the predicted S-P structures indicate the structure complexity of these compounds, such as the lattice distortions.

To understand the configuration of $TiFe_{1.5}Sb$ and $MCo_{1.33}Sn$ more intuitively, we perform the symmetry operations on the ground state structure and transform it into a cubic structure (the transformation matrix is $[3-1-1, -1\ 3-1, -1-1\ 3]$ and $[4\ 2-1, 2\ 4\ 1, 2-2\ 1]$). The transformed unit cell is shown in Figs. 2(a) and 2(b). By observing the lattices of $TiFe_{1.5}Sb$ and $MCo_{1.33}Sn$, we find that they are

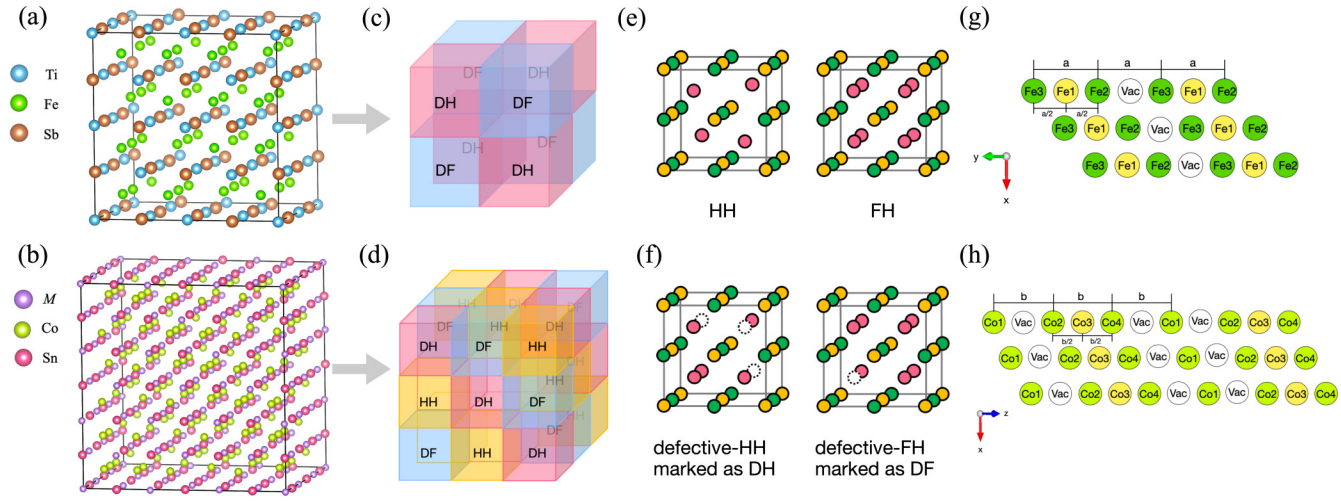

FIG. 2. Theoretically predicted $TiFe_{1.5}Sb$ and $MCo_{1.33}Sn$ (M = Ti, Zr, Hf) crystal structures (a) and (b) after transformation, (c) and (d) the arrangement of substructures, (e) and (f) the atomic arrangement in the half-Heusler (HH), full-Heusler (FH), defective-HH (DH), and defective-FH (DF) substructures, and the arrangement of Y atoms (Fe or Co) viewed along (g) the z axis and (h) the y axis.

formed by the periodic arrangement of several substructures. The models of these substructures originate from HH and FH lattices, as shown in Figs. 2(e) and 2(f). There are ideal HH and FH lattices and DH and DF lattices. For DH and DF, they include one Y interstitial and Y vacancy at the 4d ($\frac{3}{4}$, $\frac{3}{4}$, $\frac{3}{4}$) Wyckoff site, respectively. The lattice of $TiFe_{1.5}Sb$ is composed of two substructures of DH and DF [Figs. 2(a) and 2(c)], while $MCo_{1.33}Sn$ consists of three substructures of DH, DF, and HH [Figs. 2(b) and 2(d)]. The regular stacking of these substructures gives rise to the intriguing formation of second- and third-order Rubik's-cube-like structures in $TiFe_{1.5}Sb$ and $MCo_{1.33}Sn$.

From the local geometry structures in the lattice parts [Figs. 2(e) and 2(f)] of $TiFe_{1.5}Sb$ and $MCo_{1.33}Sn$, the X (Ti and M) and Z (Sb and Sn) atoms built the NaCl-type lattice, and the Y atom (Fe and Co) is coordinated by four X (Ti, Zr, Hf) and four Z (Sb, Sn) atoms. Since the Y occupations are different from those in the HH and FH lattices [Figs. 2(e) and 2(f)], we focus on the arrangement rules of Y atoms. In the crystal structure of $TiFe_{1.5}Sb$, there are three nonequivalent Fe sites, denoted as Fe1, Fe2, and Fe3, shown in Fig. 2(g). The first neighbor of each Fe atom consists of four Ti and four Sb atoms with the same bond length of ∼2.61 Å. For the second nearest neighbors, there is a difference: Fe1 is surrounded by six Fe atoms (three Fe2 and three Fe3), and Fe2 and Fe3 are surrounded by three Fe1 atoms, as shown in Fig. S5 in the Supplemental Material [67]. The second nearest Fe-Fe bond lengths are all 3.01 Å. By comparing the neighbors of Fe atoms with those of Y atoms in HH/FH (Fig. S3 in the Supplemental Material [67]), we can see that Fe2 and Fe3 are periodically arranged within the lattice as in the TiFeSb HH lattice [Fig. 2(g)], occupying the 4c ($\frac{1}{4}$, $\frac{1}{4}$, $\frac{1}{4}$) Wykoff site. As an interstitial atom, Fe1 occupies the site between Fe3 and Fe2, situated at the half position of 4d ($\frac{3}{4}$, $\frac{3}{4}$, $\frac{3}{4}$) Wyckoff site [Fig. 2(g)]. The neighboring atoms of Fe1 resemble those of Y atoms in FH, whereby the second nearest neighbors comprise six Y atoms (Fig. S5 in the Supplemental Material [67]). This suggests that the bonding behavior of Fe1 is likely to associate with that of FH. Thus, we conclude that the formation of the $TiFe_{1.5}Sb$ S-P semiconductor is a result of the migration of the extra Y (Fe) atoms to occupy half of the Y vacancy (Wyckoff site 4d) of HH [Fig. 2(g)], which can be written as $TiFe_{1.5}Sb = TiFeSb + \frac{1}{2}$ Fe. In $MCo_{1.33}Sn$ [Fig. 2(b)], there are four nonequivalent Co atoms [Fig. 2(h)], named Co1, Co2, Co3, and Co4. Each Co is eight coordinated with four M atoms and four Sn atoms with a bond length of 2.73 Å. The second neighbor among Co atoms (except Co1) has a bond length of 3.15 Å (Fig. S6 in the Supplemental Material [67]). From the distribution of Co atoms [Fig. 2(h)], Co1, Co2, and Co4 atoms are periodically arranged as in the MCoSn HH crystal structure, and Co3 as the interstitial atom appears between Co2 and Co4. The bonding environment around Co3 confirms the FH environment. Like $TiFe_{1.5}Sb$, $MCo_{1.33}Sn$ can also be written as $MCo_{1.33}Sn = MCoSn + \frac{1}{3}$ Co, which means $MCo_{1.33}Sn$ is formed due to the Y atoms (Co) migration to $\frac{1}{3}$ of the Y vacancy of HH [Fig. 2(h)]. The forming of DF and DH or the unusual atomic occupations leads to the stability of the structures of off-stoichiometry compounds. The formation of this new structure is an important guide for expanding the research scope of Heusler system.

B. Electronic structures

In HH and FH compounds, the electronic structures are strongly correlated to the VEC [73]. As we know, HH with 18e and FH with 24e are semiconductors; changing the VEC to a different value mostly causes the compounds to lose their semiconductor properties and the emergence of magnetism [74]. For the $TiFe_{1+x}Sb$ and $MCo_{1+x}Sn$ systems (Table I), their HH systems (TiFeSb and MCoSn) all have VEC = 17, and the FH systems ($TiFe_2Sb$ and MCo_2Sn) have VEC = 25 and 26, respectively. By calculating the VEC of the predicted ground state, we find that the VEC of $TiFe_{1.5}Sb$ and $MCo_{1.33}Sn$ is 21 (4 [Ti ($3d^2\,4s^2$)] + 1.5 × 8 [Fe ($3d^6\,4s^2$)] + 5 [Sb ($5s^2\,5p^3$)]) and 20 (4 [Ti ($3d^2\,4s^2$)] + $\frac{4}{3}$ × 9 [Co ($3d^7\,4s^2$)] + 4[Sn ($5s^2\,5p^2$)]), respectively. We can see that they have an average of 6 electrons per atom

TABLE I. The VEC of HH/FH compounds and the predicted compounds.

HH/FH	VEC	Predict	VEC
TiFeSb	17	$TiFe_{1.5}Sb$	21
$TiFe_2Sb$	25		
(Ti/Zr/Hf)CoSn	17	$(Ti/Zr/Hf)Co_{1.33}Sn$	20
$(Ti/Zr/Hf)Co_2Sn$	26		

$[21/(1+1.5+1)=6$ and $20/(1+\frac{4}{3}+1)=6]$, indicating S-P semiconductors.

We calculate the electron structures and DOS of $TiFe_{1.5}Sb$ and $MCo_{1.33}Sn$ (Fig. 3). We find that $TiFe_{1.5}Sb$, $TiCo_{1.33}Sn$, $ZrCo_{1.33}Sn$, and $HfCo_{1.33}Sn$ are all S-P semiconductors, with band gaps of 0.67, 0.11, 0.13, and 0.002 eV, respectively. The calculated band gap of $TiFe_{1.5}Sb$ is like the previously reported value (0.64 eV) [33]. The PBE functional usually underestimates their band gaps, and HSE06 and GW could correct them. However, these methodologies are time consuming even for a very simple system. From previous studies on the electrical properties of TE materials [75,76], HSE06 does obtain the better band gap than that from PBE calculations. Fortunately, the HSE calculated band features around the Fermi level [the band edges of valence band maximum (VBM) and the conduction band minimum] show no difference to those using PBE. It is well known that the TE properties strongly depend on the behavior of charge carriers near the Fermi level. Therefore, the PBE-calculated band structures are still reasonable for the HH TE property calculations, like most theoretical simulations in Heusler compounds [65,77,78].

From the band structures (Fig. 3), we find that the VBM lies at the Γ point in both $TiFe_{1.5}Sb$ and $MCo_{1.33}Sn$, and there are two flat bands in the conduction band above the Fermi level. From the projected DOS, we find that the flat conduction bands are contributed by Fe or Co atoms.

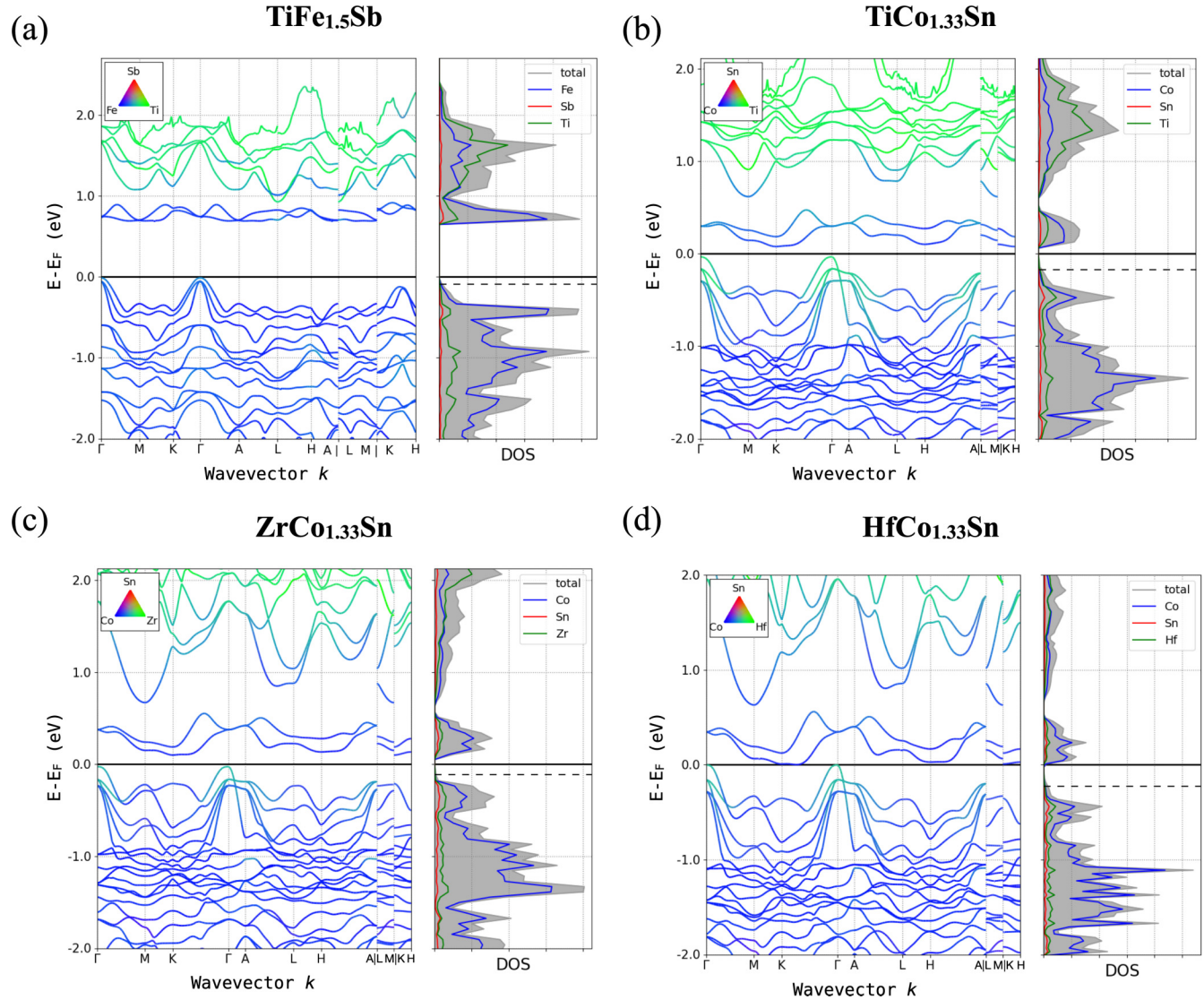

FIG. 3. Atom-resolved electronic band structures and density of states (DOS) for (a) $TiFe_{1.5}Sb$, (b) $TiCo_{1.33}Sn$, (c) $ZrCo_{1.33}Sn$, and (d) $HfCo_{1.33}Sn$. The green, blue, and red lines are represented X, Y, and Z atom contributions to the energy band. The projection of an element on the band is distinguished by color (the RGB value). The black lines represent the E_F position.

Additionally, states below the flat bands are mainly contributed by Fe (Co), and the states above the flat bands are contributed by Ti/Zr/Hf. The states of Z (Sb or Sn) atoms lie deep in the valence band and have no contribution near the Fermi level (Fig. 3). The presence of flat bands above the Fermi level indicates a large band effective mass, which is detrimental to the carrier mobility. However, the light band at the VBM with high band convergence suggests that the *p*-type material may have high TE properties [24]. Thus, our theoretically predicted $TiFe_{1.5}Sb$ and $MCo_{1.33}Sn$ compounds have the potential to serve as effective *p*-type TE materials.

C. Orbital analysis

Since those S-P semiconductors ($TiFe_{1.5}Sb$ and $MCo_{1.33}Sn$) are derived from HH and FH compounds, figuring out the bonding rules in HH and FH will help us analyze their S-P semiconducting behaviors, for a detailed schematic illustration, see the Supplemental Material [67] (see also Refs. [79–81] therein). It is well known that HH with 18e and FH with 24e are semiconductors, and the difference between these two kinds of compounds is the way to form the band gaps using orbitals. The band gap of HH is produced by the hybridization of the *d* orbitals of X-Y, and the Fermi energy level is located between the bonding and antibonding states (Fig. S7(a) in the Supplemental Material [67]). However, the band gap of FH is formed by the hybridization of the *d* orbitals of Y-Y, and the Fermi energy level is between the antibonded states of t_{1u} and e_u (Fig. S7(b) in the Supplemental Material [67]). Therefore, the band gap of HH is often much larger than that of FH [74,79,82].

Like HH or FH, the bonding behavior of the $TiFe_{1.5}Sb$ (VEC = 21) semiconductor can be understood using similar rules. From the atom-projected DOS of three nonequilibrium Fe atoms in $TiFe_{1.5}Sb$ [Fig. 4(a)], we find that t_{2g} of Fe1 is only distributed below the Fermi level, and e_g is distributed on both sides of the Fermi level. The COHP is also given to investigate the bonding behaviors between atoms [Fig. 4(b)], in which the negative and positive COHP values indicate bonding and antibonding interactions, respectively, and the values represent the strength of the interactions. The COHP result shows that the antibonding of Fe1 appears not only in the conduction band above the Fermi level but also in the valence band below the Fermi level [the black arrow in Fig. 4(b)]. This means the Fermi level locates between the two antibonding states, which is also a character of the FH bonding rule, as we discussed in the Supplemental Material [67]. This bonding behavior indicates that Fe1 is indeed in the local environment of FH.

Based on the structural analysis described above, $TiFe_{1.5}Sb$ can be interpreted as $[TiFeSb] + \frac{1}{2}$ Fe. Since the unit cell formula of $TiFe_{1.5}Sb$ is $Ti_2Fe_3Sb_2$, the formula can be written as $Ti_2Fe_3Sb_2 = 2[TiFeSb] + Fe$, in which Fe [the Fe1 atom in Fig. 2(g)] can be recognized as an interstitial atom in the TiFeSb matrix to form the local FH $[TiFe_2Sb]$ substructure. Thus, $Ti_2Fe_3Sb_2 = [TiFeSb] + [TiFeSb] + Fe1 = [TiFeSb] + [TiFe_2Sb]$. Therefore, according to the preceding DOS and COHP analysis, the bonding diagram (electrons transfer) can be separated into two connected steps [Figs. 4(c) and 4(d)]: (1) When Fe1 enters the HH [TiFeSb] substructure (VEC = 17), the hybridization forms the bonding states (the double-degenerate e_g and triple-degenerate t_{2g}) and the antibonding states (the double-degenerate e_g^* and triple-degenerate t_{2g}^*). Thus, the FH $[TiFe_2Sb]$ substructure (VEC = 25) is formed, and the corresponding Fermi level [the solid pink line in Fig. 4(c)] is above the antibonding state e_g^*. (2) Then the $[TiFe_2Sb]$ substructure will further interact with the rest of the [TiFeSb] substructure. An electron in the e_g^* state of $[TiFe_2Sb]$ will fill the hole in the t_{2g} state of [TiFeSb] [the black dashed arrow in Fig. 4(d)], forming the 18e HH $[TiFeSb]^-$ and 24e FH $[TiFe_2Sb]^+$ substructures [Fig. 4(d)]. The Fermi levels of HH and FH experience upward and downward alignments, respectively, resulting in a new position represented by the pink dotted line [Fig. 4(d)]. The shift leads to the emergence of a band gap in the $TiFe_{1.5}Sb$ compound, which exhibits semiconductor behavior. Therefore, the semiconductor behavior of $TiFe_{1.5}Sb$ is due to the redistribution of electrons between the two HH and FH substructures.

For $MCo_{1.33}Sn$, taking $ZrCo_{1.33}Sn$ as an example, combining the results of its DOS and COHP [Figs. 4(e) and 4(f)], it can be seen that t_{2g} states of Co3 are distributed below the Fermi level, and bonding and antibonding states of e_g are distributed on both sides of the Fermi level. The Fermi level appears within the two antibonding states [the black arrow in Fig. 4(f)], which illustrates that the interstitial Co3 in the HH structure locates in the local FH bonding environment. From the structure and DOS analysis, Co3 also exists as an interstitial atom [Fig. 2(h)] to donate electrons. The unit cell formula of $MCo_{1.33}Sn$ is $M_3Co_4Sn_3$, which can be understood as a combination of $M_3Co_4Sn_3 = 3[MCoSn] + Co3 = 2[MCoSn]^- + [MCo_2Sn]^{2+}$, and the bonding diagram is shown in Figs. 4(g) and 4(h): Filling Co3 in the HH [ZrCoSn] substructure (VEC = 17) induces the formation of the FH $[ZrCo_2Sn]$ substructure (VEC = 26) [Fig. 4(g)]. Then the two electrons in 26e $[ZrCo_2Sn]$ transfer to the neighboring two 17e [ZrCoSn] [the black dashed arrows in Fig. 4(h)], forming two 18e $[ZrCoSn]^-$ and one 24e $[ZrCo_2Sn]^{2+}$ substructures. After the electron transfer, the Fermi level aligns to a new position [the pink dotted line in Fig. 4(h)] and the band gap appears. Our electronic structures provide the perspective of bonding and electron transfer in the system. We can find that the partial distribution of interstitial Y atoms (Fe or Co) causes the electrons in the system to be redistributed between the HH and FH substructures, resulting in the shift of the Fermi level and opening of the band gap. Such a distribution leads to the stable mixture structures using HH and FH.

D. TE properties

1. Thermal properties

The intrinsic high thermal conductivity of HH and FH is the main obstacle for them to achieve the high TE figure of merit. In general, the tunable vacancy concentration in the off-stoichiometry compounds ($Nb_{0.8}CoSb$, $Ti_{0.75}NiSb$ [83]) can facilitate the thermal conductivity decrease through phonon scattering and lattice softening mechanisms [26]. Since low thermal conductivity is a crucial factor in identifying high-performing TE materials, it is necessary to investigate the thermal properties of our predicted S-P semiconductors. From the phonon calculations, the phonon dispersions of $TiFe_{1.5}Sb$

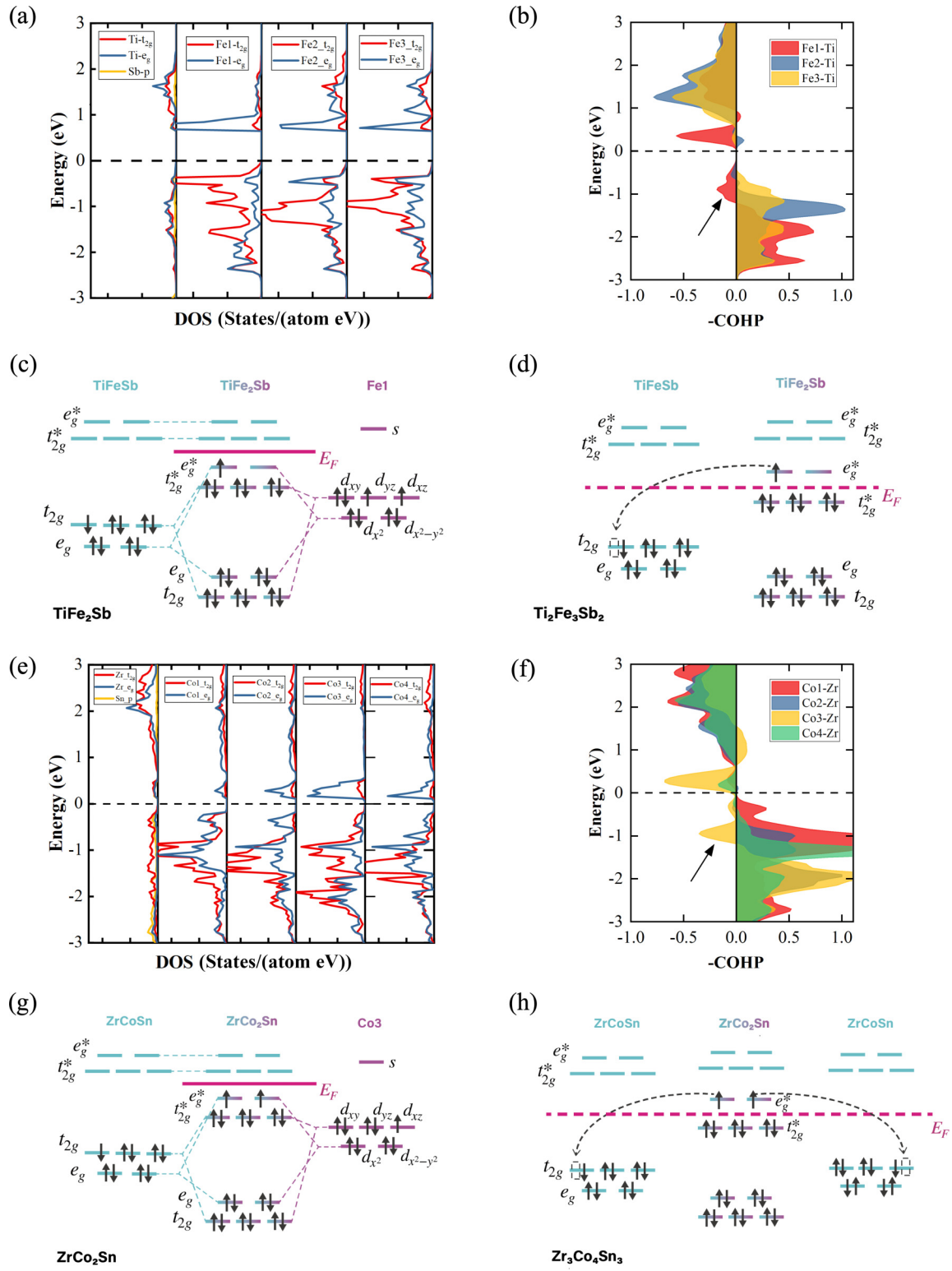

FIG. 4. Atom-resolved density of states (DOS) and crystal orbital Hamiltonian population (COHP) of (a) and (b) $TiFe_{1.5}Sb$ and (e) and (f) $ZrCo_{1.33}Sn$. Schematic illustration of molecular orbital (MO) diagram in forming (c) and (d) $TiFe_{1.5}Sb$ and (g) and (h) $ZrCo_{1.33}Sn$. The black dashed arrows in MO [(d) and (h)] represent the electron transfer process from full-Heusler (FH) to half-Heusler (HH) substructure.

and $MCo_{1.33}Sn$ (Fig. 5) do not show imaginary phonon frequencies, indicating the thermodynamical stability of these structures. For $TiFe_{1.5}Sb$, the heavy atom Sb mainly contributes to the low-frequency region <6 THz, while the high-frequency region is dominated by the light Ti and Fe atoms [Fig. 5(a)]. For $MCo_{1.33}Sn$ [Figs. 5(b)–5(d)], as the M site is changed from Ti to Zr to Hf, the atomic mass is increasing. We notice that the atom contributions to the phonons are significantly changed: The contribution of M atoms to the optical modes gradually shifts from the

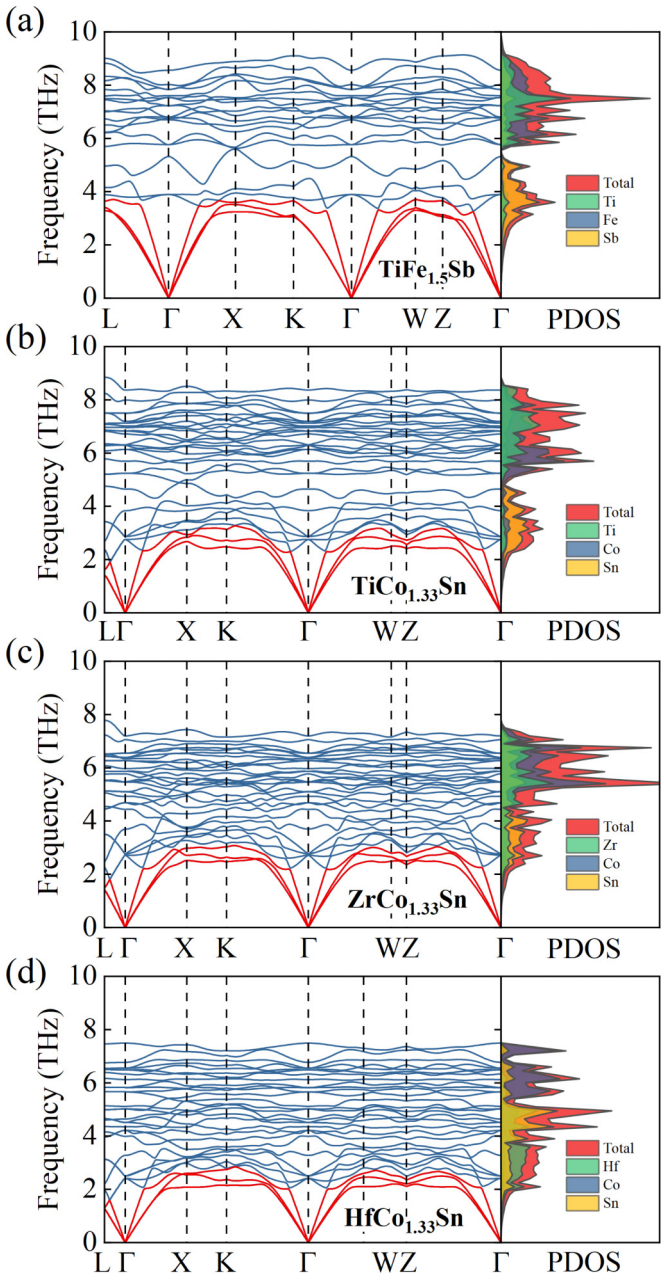

FIG. 5. Phonon dispersions and phonon density of states (PDOS) of (a) $TiFe_{1.5}Sb$, (b) $TiCo_{1.33}Sn$, (c) $ZrCo_{1.33}Sn$, and (d) $HfCo_{1.33}Sn$ along the high-symmetry pathways in their corresponding Brillouin zones. Optical branches are shown in blue and acoustic in red. The contributions of X, Y, and Z atoms in PDOS are shown in green, blue, and yellow.

high-frequency region of M = Ti to the low-frequency region of M = Hf. Thus, as the acoustic modes are predominantly contributed by the heaviest atom in the compound [84], the highest frequencies of acoustic branches of M = Ti, Zr, and Hf decrease to 3.26, 3.08, and 2.71 THz, respectively. Thus, the weak acoustic branches by shifting from Ti to Hf in $MCo_{1.33}Sn$ will lead to a great impact on κ_l.

Based on the phonon dispersions, we can extract the Debye temperatures, phonon velocities, and Grüneisen parameters [85], as shown in Table II. From the table, we can see that

TABLE II. The average transverse acoustic (TA/TA′) and longitudinal acoustic (LA) Debye temperature ($\Theta_{TA/TA'/LA}$) (K), phonon velocities ($v_{TA/TA'/LA}$) (m/s), and Grüneisen parameters of $TiFe_{1.5}Sb$ and $MCo_{1.33}Sn$ (M = Ti, Zr, Hf).

Candidates	Θ_{TA}	$\Theta_{TA'}$	Θ_{LA}	v_{TA}	$v_{TA'}$	v_{LA}	γ
$TiFe_{1.5}Sb$	158.37	168.81	178.15	3352.9	3652.1	6139.4	1.02
$TiCo_{1.33}Sn$	128.42	139.43	156.79	2838.2	3103.0	5682.2	1.07
$ZrCo_{1.33}Sn$	123.39	137.11	147.89	2826.7	3050.4	5452.8	1.09
$HfCo_{1.33}Sn$	108.43	121.73	130.44	2577.9	2757.6	5006.7	1.13

the Debye temperatures and acoustic phonon velocities gradually decrease from $TiFe_{1.5}Sb$ to $HfCo_{1.33}Sn$. This is due to the strong couplings between acoustic and optical modes in $MCo_{1.33}Sn$ pushing the acoustic branches lower. Correspondingly, the Grüneisen parameters (γ) show the opposite trend, in which $HfCo_{1.33}Sn$ has the largest γ (1.13). In these S-P compounds, in addition to the increased atomic mass of the X atom in $MCo_{1.33}Sn$, the disorder occupations of Y atoms in the geometry (Fig. 2) induce the complicated geometry structures and weak interatomic interactions (or the longer interatomic distances), which leads to the low Debye temperature, phonon group velocity, and relatively large Grüneisen parameters. In principle, the low Debye temperature and large γ value would suggest low lattice thermal conductivity [8,86].

The lattice thermal conductivity calculations can be calculated by solving the phonon BTEs (Fig. 6). In principle, the lattice thermal conductivity depends on the P3 and higher-order scatterings, such as the four-phonon (P4) scatterings. However, authors of many studies have demonstrated that the P4 interactions have a very weak influence on the systems without acoustic-optical band gaps [87–90]. From our phonon calculations of those predicted S-P compounds, they do not show such an acoustic-optical band gap, which suggests weak P4 interactions. Nevertheless, since the weighted P3 and P4 phase spaces can be used to discuss the importance of P3 and P4 effects [88,91], we perform such calculations of $TiFe_{1.5}Sb$ (see Fig. S9 in the Supplemental Material [67]). It turns out

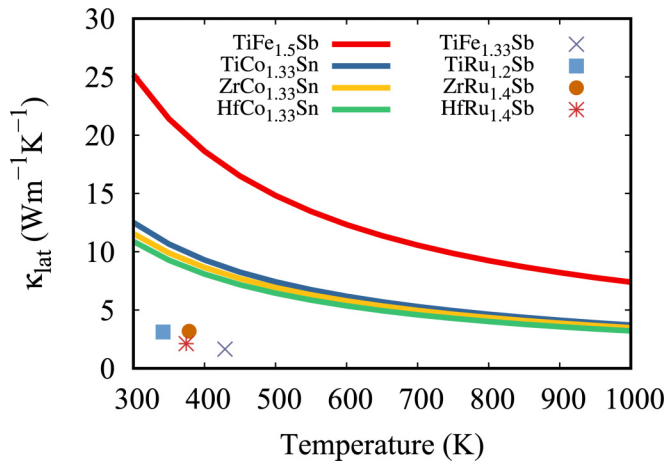

FIG. 6. The lattice thermal conductivities of $TiFe_{1.5}Sb$ and $MCo_{1.33}Sn$ (M = Ti, Zr, and Hf). The experimental data are extracted from Refs. [36–38,49].

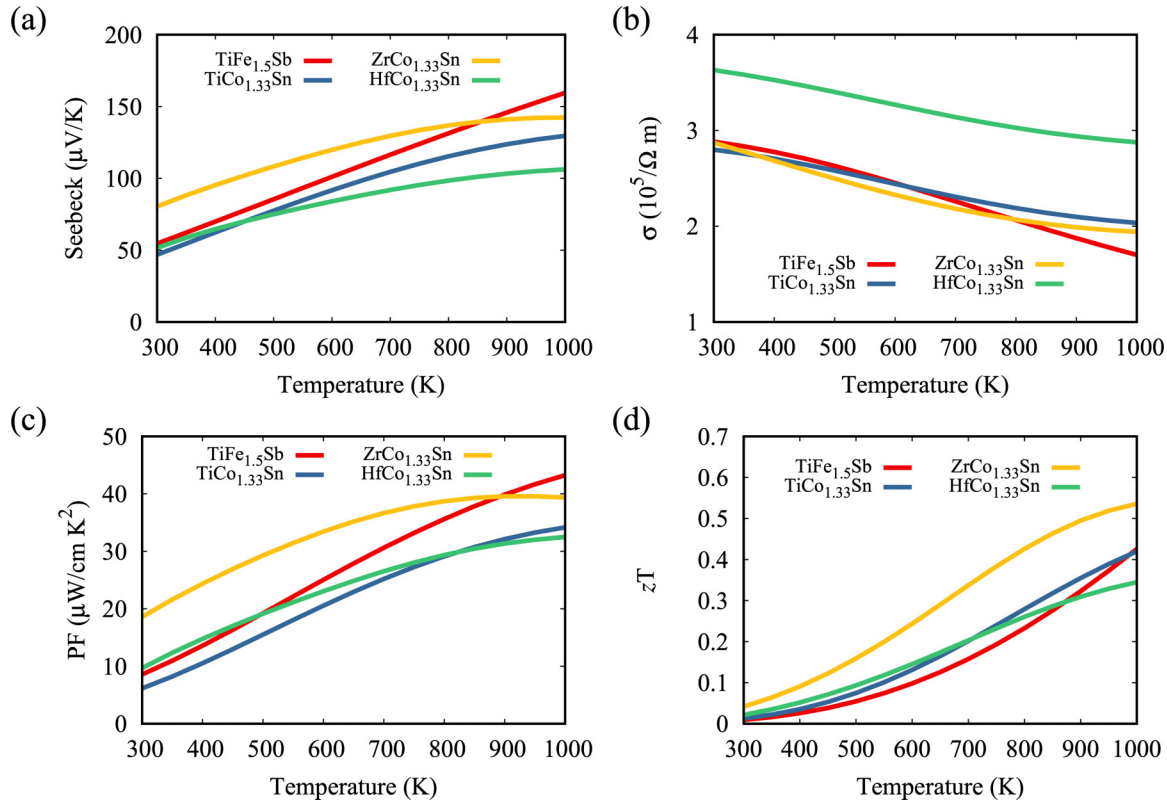

FIG. 7. (a) Temperature-dependent Seebeck coefficients, (b) electrical conductivities, (c) power factors, and (d) zT of p-type $TiFe_{1.5}Sb$ and $MCo_{1.33}Sn$.

that the P4 phase space is significantly smaller than that of P3 phase space within the low-frequency region. Since the low frequency plays an important role in the thermal conduction, it is the P3 and not the P4 interactions that dominate the lattice thermal conductivity. It is consistent with the previous HH studies [45,92,93]. Therefore, we can safely ignore the effects of time-consuming P4 scattering effects in the S-P Heusler systems. As a consequence, the thermal conductivities of $MCo_{1.33}Sn$ (12.5 W/mK for $TiCo_{1.33}Sn$, 11.6 W/mK for $ZrCo_{1.33}Sn$, and 10.8 W/mK for $HfCo_{1.33}Sn$ at 300 K) are much lower than that of the $TiFe_{1.5}Sb$ compound (25.2 W/mK at 300 K) (Fig. 6). However, our calculated lattice thermal conductivities are higher than those from the experimental measurements: <4 W/mK at 300 K for $TiFe_{1.33}Sb$ [49] and $MRu_{1+x}Sb$ [36–38] (the points in Fig. 6). This is due to possible defects and impurities in the experimentally synthesized compounds. These defects will strongly scatter phonons and decrease the lattice thermal conductivities. Nevertheless, compared with the traditional HH and FH alloys, such as the thermal conductivities of NbFeSb (16 W/mK [24]) and VFe_2Al (38 W/mK [51]), we can find that S-P semiconductors do have low thermal conductivity.

2. *Electrical transport properties*

Using electronic band structures of $TiFe_{1.5}Sb$ and $MCo_{1.33}Sn$ S-P semiconductors, we can calculate their electrical transport properties (Fig. 7) by solving the BTEs using the rigid band approximation and the CRTA ($\tau_{CRTA} = 10$ fs). From the PFs with the chemical potential (μ) (see Fig. S10 in the Supplemental Material [67]), we can see the PFs of p-type $TiFe_{1.5}Sb$ and $MCo_{1.33}Sn$ are much higher than those of n-type, which agrees with the results from band structure discussions. To understand the high PF, we concentrate on the electrical properties (S and σ) at the optimal carrier concentration ($n \approx 10^{21}$ cm^3) (for detail of the properties, see Table S3 in the Supplemental Material [67]). To achieve this optimal carrier concentration, it is suggested that the Y self-dopant should introduce 0.1 electron per cell in $TiFe_{1.5}Sb$ and $MCo_{1.33}Sn$.

Figures 7(a) and 7(b) show the Seebeck coefficient S and electrical conductivity σ for $TiFe_{1.5}Sb$ and $MCo_{1.33}Sn$ at the optimal carrier concentration. The Seebeck coefficient mainly depends on the DOS effective mass and carrier concentration, as is illustrated in the Mott equation [94]:

$$S = \frac{8\pi^2 k_B^2}{3eh^2} m_d^* T \left(\frac{\pi}{3n}\right)^{2/3}, \tag{4}$$

where k_B is the Boltzmann constant, h is the Plank constant, and m_d^* is the DOS effective mass. The Seebeck coefficient of $TiFe_{1.5}Sb$ increases significantly with increasing temperature, from 55 to 161 μV/K [Fig. 7(a)], while for $MCo_{1.33}Sn$, as the mass of M atoms increases, the trend S of them is $ZrCo_{1.33}Sn > TiCo_{1.33}Sn > HfCo_{1.33}Sn$. According to Eq. (4), the high m_d^* leads to a large Seebeck coefficient at the same charge carrier concentration. We notice that, for the three compounds, their optimal concentrations are similar. Since $ZrCo_{1.33}Sn$ has a larger DOS effective mass m_{dp}^* ($m_{dp}^* = 3.22\ m_e$) than $TiCo_{1.33}Sn$ ($m_{dp}^* = 3.04\ m_e$) and $HfCo_{1.33}Sn$

($m^*_{dp} = 2.79\ m_e$), $ZrCo_{1.33}Sn$ shows the highest Seebeck coefficient.

Good electrical properties also require high electrical conductivity. The electrical conductivity is proportional to the carrier concentration (n) and carrier mobility (μ): $\sigma = ne\mu$, where μ is inversely proportional to the conductivity effective mass of band ($\mu \propto \tau_{CRTA}/m^*_b$). Therefore, $HfCo_{1.33}Sn$ has the largest electrical conductivity [Fig. 7(b)] due to the smallest band effective mass ($m^*_{bn} = 1.09\ m_e$) and large carrier concentration (3.18×10^{21} cm^{-3}). As a result, $ZrCo_{1.33}Sn$ demonstrates superior PFs [Fig. 7(c)] throughout a wide temperature range due to its reasonable Seebeck coefficient and electrical conductivity, reaching a maximum PF value of 39 $\mu W/cm\ K^2$. On the other hand, $TiFe_{1.5}Sb$ exhibits an even higher PF at high temperature (43 $\mu W/cm\ K^2$ at 1000 K), primarily due to its elevated Seebeck coefficient at high temperature.

3. TE performance

Traditional 18e HH systems [typical systems of MNiSn (M = Ti, Zr, Hf) and RFeSb (R = V, Nb, Ta)] are considered TE materials [10] with zT values above unity in recent years. However, for the FH system, only VFe_2Al is used as a TE material with an extremely small peak zT value of 0.13 [51]. With the electrical properties and thermal conductivities, we can evaluate the zT values [Fig. 7(d)] of our predicted S-P semiconductors ($TiFe_{1.5}Sb$, $TiCo_{1.33}Sn$, $ZrCo_{1.33}Sn$, and $HfCo_{1.33}Sn$). Over the temperature range of 300–1000 K, the zT value gradually increases with increasing temperature. The zT values of $TiFe_{1.5}Sb$, $TiCo_{1.33}Sn$, $ZrCo_{1.33}Sn$, and $HfCo_{1.33}Sn$ reach maximum values of 0.43, 0.42, 0.54, and 0.35, respectively. Although $HfCo_{1.33}Sn$ possesses the lowest lattice thermal conductivity, its zT value is not the highest among these S-P semiconductors. For $ZrCo_{1.33}Sn$, the combination of the highest PF and relatively low thermal conductivity leads to the largest zT value (0.54). Although its zT value is not comparable with those of well-known HH compounds (such NbFeSb, $zT = 1.6$ [23]), it is even higher than those of recently developed S-P Heusler compounds ($zT \sim 0.4$ in $MRu_{1.5}Sb$, M = Ti, Zr, Hf). Considering that there is still a space for further reduction in κ_l by introuducing the self-dopants to scatter phonons in $ZrCo_{1.33}Sn$, the further improvement of zT in the compound can be achieved in future.

Even though the lattice thermal conductivities of these S-P semiconductors are already lower than those in the HH or FH compounds, they are still quite larger than those of compounds with intrinsic low lattice thermal conductivities (such as SnSe, 0.4 W/mK at 923 K [95]). On the other hand, the experimental measurements suggest the possibly lower lattice thermal conductivity with introducing various defects (Refs. [36–38]). The high zT values of S-P semiconductors indicate that it is possible to achieve high p-type TE properties in Heusler systems. The higher zT of our predicted S-P semiconductors not only expands the usage of FH compounds in TE materials but also provides a distinct way to improve the TE properties of Heusler compounds.

IV. CONCLUSIONS

In summary, we focus on the Ti-Fe-Sb and M-Co-Sn (M = Ti, Zr, Hf) Heusler systems, identifying the thermodynamically stable phases of $TiFe_{1.5}Sb$ and $MCo_{1.33}Sn$. The off-stoichiometry Heusler compounds exhibit VECs of 21 and 20, classifying as S-P semiconductors. From the lattice structure analysis, we find, in addition to the well-known HH and FH local geometries, DH and DF substructures are also located in the lattices. These substructures arise due to the partial occupation of Y atoms (Fe or Co) at the 4d Wyckoff site. The regular stacking of these substructures gives rise to the intriguing formation of second- and third-order Rubik's-cube-like structure in $TiFe_{1.5}Sb$ and $MCo_{1.33}Sn$. By analyzing DOS and COHP, we have clarified the bonding behaviors of these predicted off-stoichiometry S-P HH semiconductors. The band gap originates from the redistribution of electrons between the HH and FH substructures, resulting in the alignment of the Fermi level within the band gap. The unique configuration (or the arrangement of Y atoms) plays an important role in stabilizing the lattices of these systems and suppress the lattice thermal conductivity to 12.5 W/mK for $TiCo_{1.33}Sn$, 11.6 W/mK for $ZrCo_{1.33}Sn$, and 10.8 W/mK for $HfCo_{1.33}Sn$ at 300 K, which are lower than those of traditional HH and FH compounds. In combining the electrical properties, p-type $ZrCo_{1.33}Sn$ exhibits a zT value of 0.54 at 1000 K, which is attributed to its high PF and low thermal conductivity. In addition to discovering HH candidates, in this paper, we extensively discuss the physical mechanisms of bonding behavior of these S-P Heusler systems, aiming to comprehend their semiconductor behavior and possible TE optimization method. This provides theoretical guidance for the exploration of more S-P semiconductors with superior TE performance.

ACKNOWLEDGMENTS

Y.Z. acknowledges financial support from the program of "Distinguished Expert of Taishan Scholar" (No. tstp20221124). The supercomputing services from Center for Computational Science of CASHIPS, the ScGrid of Supercomputing Center, Computer Network Information Center of Chinese Academy of Science, AM-HPC, and Hefei advanced computing center are gratefully acknowledged for high-performance computing.

[1] F. Heusler, W. Starck, and E. Haupt, Magnetisch-chemische studien, Verh. Dtsch. Phys. Ges. **5**, 219 (1903).

[2] T. Zhu, C. Fu, H. Xie, Y. Liu, and X. Zhao, High efficiency half-Heusler thermoelectric materials for energy harvesting, Adv. Energy Mater. **5**, 1500588 (2015).

[3] J. J. Gutiérrez Moreno, J. Cao, M. Fronzi, and M. H. N. Assadi, A review of recent progress in thermoelectric materials through computational methods, Mater. Renew. Sustain. Energy **9**, 16 (2020).

[4] B. R. K. Nanda and I. Dasgupta, Electronic structure and magnetism in half-Heusler compounds, J. Phys. Condens. Matter **15**, 7307 (2003).

[5] C. Fu, T. Zhu, Y. Pei, H. Xie, H. Wang, G. J. Snyder, Y. Liu, Y. Liu, and X. Zhao, High band degeneracy contributes to high thermoelectric performance in *p*-type half-Heusler compounds, Adv. Energy Mater. **4**, 1400600 (2014).

[6] J. Ma, J. He, D. Mazumdar, K. Munira, S. Keshavarz, T. Lovorn, C. Wolverton, A. W. Ghosh, and W. H. Butler, Computational investigation of inverse Heusler compounds for spintronics applications, Phys. Rev. B **98**, 094410 (2018).

[7] M. Zeeshan and T. Nautiyal, J. van den Brink, and H. C. Kandpal, FeTaSb and FeMnTiSb as promising thermoelectric materials: An *ab initio* approach, Phys. Rev. Mater. **2**, 065407 (2018).

[8] T. Zhu, Y. Liu, C. Fu, J. P. Heremans, J. G. Snyder, and X. Zhao, Compromise and synergy in high-efficiency thermoelectric materials, Adv. Mater. **29**, 1605884 (2017).

[9] S. Anand, K. Xia, V. I. Hegde, U. Aydemir, V. Kocevski, T. Zhu, C. Wolverton, and G. J. Snyder, A valence balanced rule for discovery of 18-electron half-Heuslers with defects, Energy Environ. Sci. **11**, 1480 (2018).

[10] R. Freer, D. Ekren, T. Ghosh, K. Biswas, P. Qiu, S. Wan, L. Chen, S. Han, C. Fu, T. Zhu *et al.*, Key properties of inorganic thermoelectric materials—Tables (version 1), J. Phys. Energy **4**, 022002 (2022).

[11] M. Fava, N. H. Protik, C. Li, N. K. Ravichandran, J. Carrete, A. Van Roekeghem, G. K. H. Madsen, N. Mingo, and D. Broido, How dopants limit the ultrahigh thermal conductivity of boron arsenide: A first principles study, Npj Comput. Mater. **7**, 54 (2021).

[12] R. He, D. Kraemer, J. Mao, L. Zeng, Q. Jie, Y. Lan, C. Li, J. Shuai, H. S. Kim, Y. Liu, D. Broido, C. W. Chu, G. Chen, and Z. Ren, Achieving high power factor and output power density in *p*-type half-Heuslers $Nb_{1-x}Ti_xFeSb$, Proc. Natl. Acad. Sci. USA **113**, 13576 (2016).

[13] M. Zhou, L. Chen, C. Feng, D. Wang, and J. F. Li, Moderate-temperature thermoelectric properties of TiCoSb-based half-Heusler compounds $Ti_{1-x}Ta_xCoSb$, J. Appl. Phys. **101**, 113714 (2007).

[14] Z. Ti, S. Guo, X. Zhang, J. Li, and Y. Zhang, Thermoelectric property enhancement by merging bands in NbFeSb-based half-Heusler mixtures, J. Mater. Chem. A **10**, 5593 (2022).

[15] C. Uher, J. Yang, S. Hu, D. T. Morelli, and G. P. Meisner, Transport properties of pure and doped *M*NiSn (M = Zr, Hf), Phys. Rev. B **59**, 8615 (1999).

[16] S. Chen and Z. Ren, Recent progress of half-Heusler for moderate temperature thermoelectric applications, Mater. Today **16**, 387 (2013).

[17] R. He, H. Zhu, J. Sun, J. Mao, H. Reith, S. Chen, G. Schierning, K. Nielsch, and Z. Ren, Improved thermoelectric performance of *n*-type half-Heusler $MCo_{1-x}Ni_xSb$ (M = Hf, Zr), Mater. Today Phys. **1**, 24 (2017).

[18] R. A. Downie, D. A. Maclaren, and J. W. G. Bos, Thermoelectric performance of multiphase *X*NiSn (X = Ti, Zr, Hf) half-Heusler alloys, J. Mater. Chem. A **2**, 6107 (2014).

[19] M. Schwall and B. Balke, Phase separation as a key to a thermoelectric high efficiency, Phys. Chem. Chem. Phys. **15**, 1868 (2013).

[20] C. Yu, T. J. Zhu, R. Z. Shi, Y. Zhang, X. B. Zhao, and J. He, High-performance half-Heusler thermoelectric materials $Hf_{1-x}Zr_xNiSn_{1-y}Sb_y$ prepared by levitation melting and spark plasma sintering, Acta Mater. **57**, 2757 (2009).

[21] E. Rausch, B. Balke, J. M. Stahlhofen, S. Ouardi, U. Burkhardt, and C. Felser, Fine tuning of thermoelectric performance in phase-separated half-Heusler compounds, J. Mater. Chem. C **3**, 10409 (2015).

[22] X. Yan, W. Liu, S. Chen, H. Wang, Q. Zhang, G. Chen, and Z. Ren, Thermoelectric property study of nanostructured *p*-type half-Heuslers (Hf, Zr, Ti)$CoSb_{0.8}Sn_{0.2}$, Adv. Energy Mater. **3**, 1195 (2013).

[23] J. Yu, C. Fu, Y. Liu, K. Xia, U. Aydemir, T. C. Chasapis, G. J. Snyder, X. Zhao, and T. Zhu, Unique role of refractory Ta alloying in enhancing the figure of merit of NbFeSb thermoelectric materials, Adv. Energy Mater. **8**, 1701313 (2018).

[24] C. Fu, S. Bai, Y. Liu, Y. Tang, L. Chen, X. Zhao, and T. Zhu, Realizing high figure of merit in heavy-band *p*-type half-Heusler thermoelectric materials, Nat. Commun. **6**, 8144 (2015).

[25] K. Kudo, S. Yamada, J. Chikada, Y. Shimanuki, T. Ishibe, S. Abo, H. Miyazaki, Y. Nishino, Y. Nakamura, and K. Hamaya, Significant reduction in the thermal conductivity of Si-substituted Fe_2VAl epilayers, Phys. Rev. B **99**, 054201 (2019).

[26] K. Kimura, K. Yamamoto, K. Hayashi, S. Tsutsui, N. Happo, S. Yamazoe, H. Miyazaki, S. Nakagami, J. R. Stellhorn, S. Hosokawa *et al.*, Local structure and atomic dynamics in Fe_2VAl Heusler-type thermoelectric material: The effect of heavy element doping, Phys. Rev. B **101**, 024302 (2020).

[27] Y. Nishino, S. Deguchi, and U. Mizutani, Thermal and transport properties of the Heusler-type $Fe_2VAl_{1-x}Ge_x$ ($0 \leqslant x \leqslant 0.20$) alloys: Effect of doping on lattice thermal conductivity, electrical resistivity, and Seebeck coefficient, Phys. Rev. B **74**, 115115 (2006).

[28] F. Garmroudi, A. Riss, M. Parzer, N. Reumann, H. Müller, E. Bauer, S. Khmelevskyi, R. Podloucky, T. Mori, K. Tobita *et al.*, Boosting the thermoelectric performance of Fe_2VAl-type Heusler compounds by band engineering, Phys. Rev. B **103**, 085202 (2021).

[29] M. Hellenbrandt, The Inorganic Crystal Structure Database (ICSD)—Present and future, Crystallogr. Rev. **10**, 17 (2004).

[30] W. G. Zeier, S. Anand, L. Huang, R. He, H. Zhang, Z. Ren, C. Wolverton, and G. J. Snyder, Using the 18-electron rule to understand the nominal 19-electron half-Heusler NbCoSb with Nb vacancies, Chem. Mater. **29**, 1210 (2017).

[31] K. Xia, Y. Liu, S. Anand, G. J. Snyder, J. Xin, J. Yu, X. Zhao, and T. Zhu, Enhanced thermoelectric performance in 18-electron $Nb_{0.8}CoSb$ half-Heusler compound with intrinsic Nb vacancies, Adv. Funct. Mater. **28**, 1705845 (2018).

[32] F. Luo, J. Wang, C. Zhu, X. He, S. Zhang, J. Wang, H. Liu, and Z. Sun, 18-electron half-Heusler compound $Ti_{0.75}NiSb$ with intrinsic Ti vacancies as a promising thermoelectric material, J. Mater. Chem. A **10**, 9655 (2022).

[33] N. Naghibolashrafi, S. Keshavarz, V. I. Hegde, A. Gupta, W. H. Butler, J. Romero, K. Munira, P. Leclair, D. Mazumdar, J. Ma *et al.*, Synthesis and characterization of Fe-Ti-Sb intermetallic compounds: Discovery of a new Slater-Pauling phase, Phys. Rev. B **93**, 104424 (2016).

[34] S. Anand and G. J. Snyder, Structural understanding of the Slater-Pauling electron count in defective Heusler thermoelectric $TiFe_{1.5}Sb$ as a valence balanced semiconductor, ACS Appl. Electron. Mater. **4**, 3392 (2022).

[35] H. Huang, L. Yang, Y. Xiong, P. Qiu, T. Xing, C. Ming, Y. Y. Sun, B. Ge, X. Shi, and L. Chen, $MCo_{1.5}Sn$ (M = Ti, Zr, and Hf) ternary compounds: A class of three-quarter Heusler compounds, Mater. Today Phys. **15**, 100251 (2020).

[36] J. Zhang, Z. Dong, S. Tan, Y. Li, J. Zhang, W. Zhang, and J. Luo, Designing vacancy-filled Heusler thermoelectric semiconductors by the Slater-Pauling rule, Mater. Today Energy **27**, 101035 (2022).

[37] L. Wang, Z. Dong, S. Tan, J. Zhang, W. Zhang, and J. Luo, Discovery of a Slater-Pauling semiconductor $ZrRu_{1.5}Sb$ with promising thermoelectric properties, Adv. Funct. Mater. **32**, 2200438 (2022).

[38] Z. Dong, J. Luo, C. Wang, Y. Jiang, S. Tan, Z. Yu, K. Guo, J. Zhang, W. Zhang, Y. Zhang *et al.*, Half-Heusler-like compounds with wide continuous compositions and tunable p- to n-type semiconducting thermoelectrics, Nat. Commun. **13**, 35 (2022).

[39] V. V. Romaka, P. Rogl, L. Romaka, Y. Stadnyk, A. Grytsiv, O. Lakh, and V. Krayovskii, Peculiarities of structural disorder in Zr- and Hf-containing Heusler and half-Heusler stannides, Intermetallics **35**, 45 (2013).

[40] J. P. A. Makongo, D. K. Misra, J. R. Salvador, N. J. Takas, G. Wang, M. R. Shabetai, A. Pant, P. Paudel, C. Uher, K. L. Stokes *et al.*, Thermal and electronic charge transport in bulk nanostructured $Zr_{0.25}Hf_{0.75}$ NiSn composites with full-Heusler inclusions, J. Solid State Chem. **184**, 2948 (2011).

[41] Y. W. Chai and Y. Kimura, Nanosized precipitates in half-Heusler TiNiSn alloy, Appl. Phys. Lett. **100**, 033114 (2012).

[42] D. T. Do, S. D. Mahanti, and J. J. Pulikkoti, Electronic structure of Zr-Ni-Sn systems: Role of clustering and nanostructures in half-Heusler and Heusler limits, J. Phys. Condens. Matter **26**, 275501 (2014).

[43] N. S. Chauhan, B. Gahtori, B. Sivaiah, S. D. Mahanti, A. Dhar, and A. Bhattacharya, Modulating the lattice dynamics of n-type Heusler compounds via tuning Ni concentration, Appl. Phys. Lett. **113**, 013902 (2018).

[44] S. Guo, Z. Liu, Z. Feng, T. Jia, S. Anand, G. J. Snyder, and Y. Zhang, Prediction of improved thermoelectric performance by ordering in double half-Heusler materials, J. Mater. Chem. A **8**, 23590 (2020).

[45] S. Anand, M. Wood, Y. Xia, C. Wolverton, and G. J. Snyder, Double half-Heuslers, Joule **3**, 1226 (2019).

[46] J. C. Slater, Molecular energy levels and valence bonds, Phys. Rev. **38**, 1109 (1931).

[47] L. Pauling, Paramagnetic susceptibility to the structure, J. Am. Chem. Soc. **53**, 1367 (1931).

[48] A. Williams, V. Moruzzi, A. Malozemoff, and K. Terakura, Generalized Slater-Pauling curve for transition-metal magnets, IEEE Trans. Magn. **19**, 1983 (1983).

[49] A. Tavassoli, A. Grytsiv, G. Rogl, V. V. Romaka, H. Michor, M. Reissner, E. Bauer, M. Zehetbauer, and P. Rogl, The half Heusler system $Ti_{1+x}Fe_{1.33-x}Sb$−TiCoSb with Sb/Sn substitution: Phase relations, crystal structures and thermoelectric properties, Dalt. Trans. **47**, 879 (2018).

[50] Z. Liu, S. Guo, Y. Wu, J. Mao, Q. Zhu, H. Zhu, Y. Pei, J. Sui, Y. Zhang, and Z. Ren, Design of high-performance disordered half-Heusler thermoelectric materials using 18-electron rule, Adv. Funct. Mater. **29**, 1905044 (2019).

[51] C. S. Lue, C. F. Chen, J. Y. Lin, Y. T. Yu, and Y. K. Kuo, Thermoelectric properties of quaternary Heusler alloys $Fe_2VAl_{1-x}Si_x$, Phys. Rev. B **75**, 064204 (2007).

[52] W. Kohn, A. D. Becke, and R. G. Parr, Density functional theory of electronic structure, J. Phys. Chem. **100**, 12974 (1996).

[53] G. Kresse and D. Joubert, From ultrasoft pseudopotentials to the projector augmented-wave method, Phys. Rev. B **59**, 1758 (1999).

[54] J. P. Perdew, K. Burke, and M. Ernzerhof, Generalized gradient approximation made simple, Phys. Rev. Lett. **77**, 3865 (1996).

[55] H. J. Monkhorst and J. D. Pack, Special points for Brillouin-zone integrations, Phys. Rev. B **13**, 5188 (1976).

[56] R. Nelson, C. Ertural, J. George, V. L. Deringer, G. Hautier, and R. Dronskowski, LOBSTER: Local orbital projections, atomic charges, and chemical-bonding analysis from projector-augmented-wave-based density-functional theory, J. Comput. Chem. **41**, 1931 (2020).

[57] Q. Wu, B. He, T. Song, J. Gao, and S. Shi, Cluster expansion method and its application in computational materials science, Comput. Mater. Sci. **125**, 243 (2016).

[58] S. Hao, L. D. Zhao, C. Q. Chen, V. P. Dravid, M. G. Kanatzidis, and C. M. Wolverton, Theoretical prediction and experimental confirmation of unusual ternary ordered semiconductor compounds in Sr-Pb-S system, J. Am. Chem. Soc. **136**, 1628 (2014).

[59] Y. Zhang, V. Ozoliņš, D. Morelli, and C. Wolverton, Prediction of new stable compounds and promising thermoelectrics in the Cu-Sb-Se system, Chem. Mater. **26**, 3427 (2014).

[60] Y. Zhang, V. Blum, and K. Reuter, Accuracy of first-principles lateral interactions: Oxygen at Pd(100), Phys. Rev. B **75**, 235406 (2007).

[61] G. K. H. Madsen, J. Carrete, and M. J. Verstraete, BOLTZTRAP2, a program for interpolating band structures and calculating semi-classical transport coefficients, Comput. Phys. Commun. **231**, 140 (2018).

[62] G. K. H. Madsen and D. J. Singh, BOLTZTRAP. A code for calculating band-structure dependent quantities, Comput. Phys. Commun. **175**, 67 (2006).

[63] S. Guo, T. Jia, and Y. Zhang, Electrical property dominated promising half-Heusler thermoelectrics through high-throughput material computations, J. Phys. Chem. C **123**, 18824 (2019).

[64] J. Yang, H. Li, T. Wu, W. Zhang, L. Chen, and J. Yang, Evaluation of half-Heusler compounds as thermoelectric materials based on the calculated electrical transport properties, Adv. Funct. Mater. **18**, 2880 (2008).

[65] J. He, M. Amsler, Y. Xia, S. S. Naghavi, V. I. Hegde, S. Hao, S. Goedecker, V. Ozoliņš, and C. Wolverton, Ultralow thermal conductivity in full Heusler semiconductors, Phys. Rev. Lett. **117**, 046602 (2016).

[66] A. M. Ganose, J. Park, A. Faghaninia, R. Woods-Robinson, K. A. Persson, and A. Jain, Efficient calculation of carrier scattering rates from first principles, Nat. Commun. **12**, 2222 (2021).

[67] See Supplemental Material at http://link.aps.org/supplemental/10.1103/PhysRevB.108.195203 for the crystal structures of ground states predicted by CE, calculated XRD pattern, analysis

of the second nearest-neighbor atoms of the Y atom in HH/FH and S-P semiconductors, the origin of the band gap in HH/FH, MRTA, scattering phase spaces, PF as a function of chemical potential, and transport parameters of S-P semiconductors. The Supplemental Material also contains Refs. [79–81].

[68] S. Baroni, S. de Gironcoli, A. D. Corso, and P. Giannozzi, Phonons and related crystal properties from density-functional perturbation theory, Rev. Mod. Phys. **73**, 515 (2001).

[69] A. Togo and I. Tanaka, First principles phonon calculations in materials science, Scr. Mater. **108**, 1 (2015).

[70] W. Li, L. Lindsay, D. A. Broido, D. A. Stewart, and N. Mingo, Thermal conductivity of bulk and nanowire $Mg_2Si_xSn_{1-x}$ alloys from first principles, Phys. Rev. B **86**, 174307 (2012).

[71] W. Li, J. Carrete, N. A. Katcho, and N. Mingo, SHENGBTE: A solver of the Boltzmann transport equation for phonons, Comput. Phys. Commun. **185**, 1747 (2014).

[72] S. Kirklin, J. E. Saal, B. Meredig, A. Thompson, J. W. Doak, M. Aykol, S. Rühl, and C. Wolverton, The Open Quantum Materials Database (OQMD): Assessing the accuracy of DFT formation energies, npj Comput. Mater. **1**, 15010 (2015).

[73] W. G. Zeier, J. Schmitt, G. Hautier, U. Aydemir, Z. M. Gibbs, C. Felser, and G. J. Snyder, Engineering half-Heusler thermoelectric materials using Zintl chemistry, Nat. Rev. Mater. **1**, 16032 (2016).

[74] T. Graf, C. Felser, and S. S. P. Parkin, Simple rules for the understanding of Heusler compounds, Prog. Solid State Chem. **39**, 1 (2011).

[75] C. N. Kuo, H. W. Lee, C. M. Wei, Y. H. Lin, Y. K. Kuo, and C. S. Lue, Ru_2NbGa: A Heusler-type compound with semimetallic characteristics, Phys. Rev. B **94**, 205116 (2016).

[76] E. H. Shourov, P. J. Strohbeen, D. Du, A. Sharan, F. C. De Lima, F. Rodolakis, J. L. McChesney, V. Yannello, A. Janotti, T. Birol, and J. K. Kawasaki, Electronic correlations in the semiconducting half-Heusler compound FeVSb, Phys. Rev. B **103**, 045134 (2021).

[77] H. Zhu, R. He, J. Mao, Q. Zhu, C. Li, J. Sun, W. Ren, Y. Wang, Z. Liu, Z. Tang *et al.*, Discovery of ZrCoBi based half Heuslers with high thermoelectric conversion efficiency, Nat. Commun. **9**, 2497 (2018).

[78] Y. Liu, C. Fu, K. Xia, J. Yu, X. Zhao, H. Pan, C. Felser, and T. Zhu, Lanthanide contraction as a design factor for high-performance half-Heusler thermoelectric materials, Adv. Mater. **30**, 1800881 (2018).

[79] C. Felser and A. Hirohata, *Heusler Alloys: Properties, Growth, Applications* (Springer, Cham, 2015).

[80] I. Galanakis and P. H. Dederichs, Origin and properties of the gap in the half-ferromagnetic Heusler alloys, Phys. Rev. B **66**, 134428 (2002).

[81] I. Galanakis, P. H. Dederichs, and N. Papanikolaou, Slater-Pauling behavior and origin of the half-metallicity of the full-Heusler alloys, Phys. Rev. B **66**, 174429 (2002).

[82] J. A. Mayer and R. Seshadri, Electron count dictates phase separation in Heusler alloys, Phys. Rev. Mater. **6**, 054406 (2022).

[83] S. Anand, K. Xia, T. Zhu, C. Wolverton, and G. J. Snyder, Temperature dependent *n*-type self doping in nominally 19-electron half-Heusler thermoelectric materials, Adv. Energy Mater. **8**, 1801409 (2018).

[84] A. Page, C. Uher, P. F. Poudeu, and A. Van Der Ven, Phase separation of full-Heusler nanostructures in half-Heusler thermoelectrics and vibrational properties from first-principles calculations, Phys. Rev. B **92**, 174102 (2015).

[85] Y. Zhang, First-principles Debye-Callaway approach to lattice thermal conductivity, J. Mater. **2**, 237 (2016).

[86] Z. Li, H. Xie, S. Hao, Y. Xia, X. Su, M. G. Kanatzidis, C. Wolverton, and X. Tang, Optical phonon dominated heat transport: A first-principles thermal conductivity study of $BaSnS_2$, Phys. Rev. B **104**, 245209 (2021).

[87] N. K. Ravichandran and D. Broido, Phonon-phonon interactions in strongly bonded solids: Selection rules and higher-order processes, Phys. Rev. X **10**, 021063 (2020).

[88] X. Song, Y. Zhao, J. Ni, S. Meng, and Z. Dai, Strong anharmonic phonon scattering and superior thermoelectric properties of Li_2NaBi, Mater. Today Phys. **31**, 100990 (2023).

[89] Y. Zhang, Z. Tong, A. Pecchia, C. Y. Yam, T. Dumitrică, and T. Frauenheim, Four-phonon and electron-phonon scattering effects on thermal properties in two-dimensional $2H-TaS_2$, Nanoscale **14**, 13053 (2022).

[90] T. Feng, L. Lindsay, and X. Ruan, Four-phonon scattering significantly reduces intrinsic thermal conductivity of solids, Phys. Rev. B **96**, 161201(R) (2017).

[91] Z. Han, X. Yang, W. Li, T. Feng, and X. Ruan, FOURPHONON: An extension module to SHENGBTE for computing four-phonon scattering rates and thermal conductivity, Comput. Phys. Commun. **270**, 108179 (2022).

[92] Z. Feng, Y. Fu, Y. Zhang, and D. J. Singh, Characterization of rattling in relation to thermal conductivity: Ordered half-Heusler semiconductors, Phys. Rev. B **101**, 064301 (2020).

[93] J. Carrete, W. Li, N. Mingo, S. Wang, and S. Curtarolo, Finding unprecedentedly low-thermal-conductivity half-Heusler semiconductors via high-throughput materials modeling, Phys. Rev. X **4**, 011019 (2014).

[94] M. Cutler, J. F. Leavy, and R. L. Fitzpatrick, Electronic transport in semimetallic cerium sulfide, Phys. Rev. **133**, A1143 (1964).

[95] L. D. Zhao, G. Tan, S. Hao, J. He, Y. Pei, H. Chi, H. Wang, S. Gong, H. Xu, V. P. Dravid *et al.*, Ultrahigh power factor and thermoelectric performance in hole-doped single-crystal SnSe, Science **351**, 141 (2016).